RARE METALS

ORIGINAL ARTICLE

Spray pyrolysis-derived W-doped MoSe₂/rGO paper-like microspheres: optimization of microstructure and mesostructure for enhanced lithium storage

Wei Wang, Jun-Yu Chen, Jie Ouyang, Hong Yin* , Ao-Jie Li,
Liang Chen, Jun-Lin Huang, Yu-Can Zhu* , Gang-Yong Li, Zhao-Hui Hou*

Abstract Two-dimensional MoSe₂ is a promising candidate for lithium-ion battery anodes. However, its conductivity and lithium storage volumetric effect still need to be optimized. In this work, W-doped MoSe₂/rGO paper-like microspheres are successfully prepared through ultrasonic spray pyrolysis, achieving optimization at both the microstructure and mesostructure to enhance the lithium storage performance of the material. Firstly, by utilizing the similar two-dimensional structure between MoSe₂ and rGO, self-assembly is achieved through spray pyrolysis, resulting in a well-defined van der Waals heterostructure at the interface on the microscale, enhancing the electron and ion transfer capability of the composite. Secondly, the mesoscale paper-like microsphere morphology provides additional volume expansion buffering space. Moreover, W-doping not only increases the interlayer spacing of MoSe₂ (0.73 nm), thereby reducing the diffusion resistance of Li⁺, but also allow for the modulation of the energy band structure of the material. Density functional theory (DFT) calculations confirm that W-doped MoSe₂/rGO exhibits the narrowest bandgap (0.892 eV). Therefore, the composite demonstrates excellent lithium storage performance, maintaining a specific capacity of 732.9 mAh·g⁻¹ after 300 cycles at a current density of 1 A·g⁻¹.

Keywords Molybdenum selenide; Heterostructure; Microspheres; Li-ion batteries; Kinetics

W. Wang, J.-Y. Chen, H. Yin*, A.-J. Li, L. Chen, J.-L. Huang, Y.-C. Zhu*, G.-Y. Li, Z.-H. Hou*
Key Laboratory of Hunan Province for Advanced Carbon-based Functional Materials, Hunan Institute of Science and Technology, Yueyang 414006, China
e-mail: Hong.yin@inl.int

Y.-C. Zhu
e-mail: 12021032@hnist.edu.cn

Z.-H. Hou
e-mail: zhaohuihou@126.com

W. Wang, J.-Y. Chen, H. Yin, A.-J. Li, L. Chen, J.-L. Huang, G.-Y. Li, Z.-H. Hou
School of Chemistry and Chemical Engineering, Hunan Institute of Science and Technology, Yueyang 414006, China

J. Ouyang
Hunan Province Key Laboratory of Materials Surface & Interface Science and Technology, Material Science and Engineering School, Central South University of Forestry and Technology, Changsha 410004, China

H. Yin
International Iberian Nanotechnology Laboratory (INL), Av. Mestre Jose Veiga, 4715-330 Braga, Portugal

1 Introduction

Transition metal selenides possess exceptional conductivity and special photoelectrochemical characteristics [1–3], rendering them a popular choice in energy storage and conversion technologies, including alkali metal ion batteries [4–9] and photoelectrocatalysis [10–14]. Particularly, when applied in lithium-ion batteries (LIBs), they have been widely studied due to their high lithium storage capacity and advantageous phase structures that promote lithium storage [15]. Examples of such materials include GeSe, NiSe, CoSe₂ and SnSe₂, which have demonstrated remarkable electrochemical performance [16–19].

Among them, MoSe$_2$ has attracted much attention in researchers due to its stable electrochemical reactivity and low solubility [20]. It exists in three different crystal forms (1T, 2H and 3R), where the most stable 2H-MoSe$_2$ block has a narrow bandgap (1.1 eV) and a large interlayer spacing (0.646 nm) [21–23]. This reduces the energy expended during electron transitions of lithium storage process, enhancing ion transport, decreasing polarization and thus boosting charge–discharge efficiency [24, 25]. Additionally, MoSe$_2$ displays both intercalation and phase transition characteristics for lithium storage, with lithium ions intercalating between the MoSe$_2$ layers and undergoing a phase transition reaction (MoSe$_2$ + 4Li$^+$ + 4e$^-$ → 2Li$_2$Se + Mo, theoretical capacity of 422 mAh·g^{-1}) [26, 27]. Despite being a semiconductor material, the conductivity of 2H-MoSe$_2$ requires improvement, and its mechanical stress is relatively weak, leading to severe volumetric effects during the lithiation process, similar to molybdenum oxide and molybdenum sulfide [28, 29].

The optimization of MoSe$_2$ for enhanced lithium storage performance can be done on both a microscopic and mesoscopic scale. For example, Yao et al. [30] used a combination of 2H-MoSe$_2$ with a graphite-like hexagonal layered structure and graphene to create microscopic van der Waals heterostructures, with the assistance of ethylenediamine, resulting in an increased volumetric capacitance. Additionally, metal doping can be used to improve the band structure of MoSe$_2$, leading to an enhancement of its energy storage capacity at the intrinsic level. Zhang et al. [31] modified the surface adsorption capacity of the material through a 1% Mn-doping. DFT analysis showed an increased electron occupancy on the Fermi level, which helped optimize the electrochemical reactions. Wang et al. [32] also employed Fe-doping to manipulate the bandgap and exploit changes in the local electronic structure to boost the electrochemical performance and durability of the material. Moreover, by blending MoSe$_2$ with carbon materials and controlling its mesoscopic morphology, the volumetric effects of MoSe$_2$ during lithium storage can be restrained [33–36]. As an example, Wu et al. developed MoSe$_2$-C nanocomposites with small particle size and large interlayer spacing through a hydrothermal process, resulting in remarkable cycling and rate performance of lithium storage by optimizing the structure [37–39].

In this work, a novel W-doped MoSe$_2$/rGO paper-like microsphere composite was successfully synthesized through an ultrasonic spray pyrolysis process. Compared to traditional composite synthesis strategies, the self-assembly mechanism in this method enables the composite to be formed with fewer layers of MoSe$_2$ while creating a volumetric buffer space in the paper-like microspheres.

Moreover, the van der Waals heterostructure of rGO and MoSe$_2$ at the microscopic interface increases the electronic and ionic transport capabilities of the material. Furthermore, the W doping adjusts the energy band structure of MoSe$_2$, boosting the conductivity and ion adsorption of the material, thereby further enhancing its structural stability and lithium storage performance.

2 Experimental

2.1 Chemicals

The reagents used in this experiment are all analytical grade chemicals and need no further treatment. Ammonium molybdate, ammonium tungstate and pure MoSe$_2$ were all provided by Aladdin Biochemical Technology Co., Ltd. Hexamethylenetetramine (HMTA) was provided by Sinopharm Chemical Reagent Co., Ltd. Graphene oxide (GO) was provided by Nanjing XFNANO Materials Tech Co., Ltd. The water used in this experiment was deionized water.

2.2 Synthesis of MoSe$_2$/rGO-x

GO was initially dispersed in 100 ml deionized water to achieve a concentration of 1 mg·ml^{-1}. Subsequently, 3.090 g ammonium molybdate and 1.051 g HMTA were dissolved in the dispersion, forming a precursor solution. This solution was then sprayed into a tubular furnace using air as the carrier gas at a flow rate of 20 L·min^{-1} and an ultrasonic frequency of 1.7 MHz. The thermal decomposition process took place at a temperature of 800 °C. The resulting spray pyrolysis product was denoted as P-MoSe$_2$/rGO-1. As a comparison, the spray pyrolysis product obtained without the addition of GO was designated as P-MoSe$_2$. P-MoSe$_2$/rGO-1 was mixed with selenium powder and subjected to annealing in an Ar-H$_2$(5%) atmosphere at 450 °C for 4 h. The product was denoted as MoSe$_2$/rGO-1. The digit represents the concentration of GO in the preparation process. For comparison purposes, MoSe$_2$ was mixed with a GO dispersion of 1 mg·ml^{-1}, followed by drying and annealing at 450 °C, resulting in the formation of the MoSe$_2$-rGO mixture. Additionally, by varying the concentration of GO to 0.5 mg·ml^{-1} and 1.5 mg·ml^{-1}, different products were obtained and denoted as MoSe$_2$/rGO-0.5 and MoSe$_2$/rGO-1.5, respectively.

2.3 Synthesis of MoSe$_2$(W x%)/rGO

GO was initially dispersed in 100 ml deionized water to achieve a concentration of 1 mg·ml^{-1}. Subsequently, 3.090 g ammonium molybdate, 1.051 g HMTA and
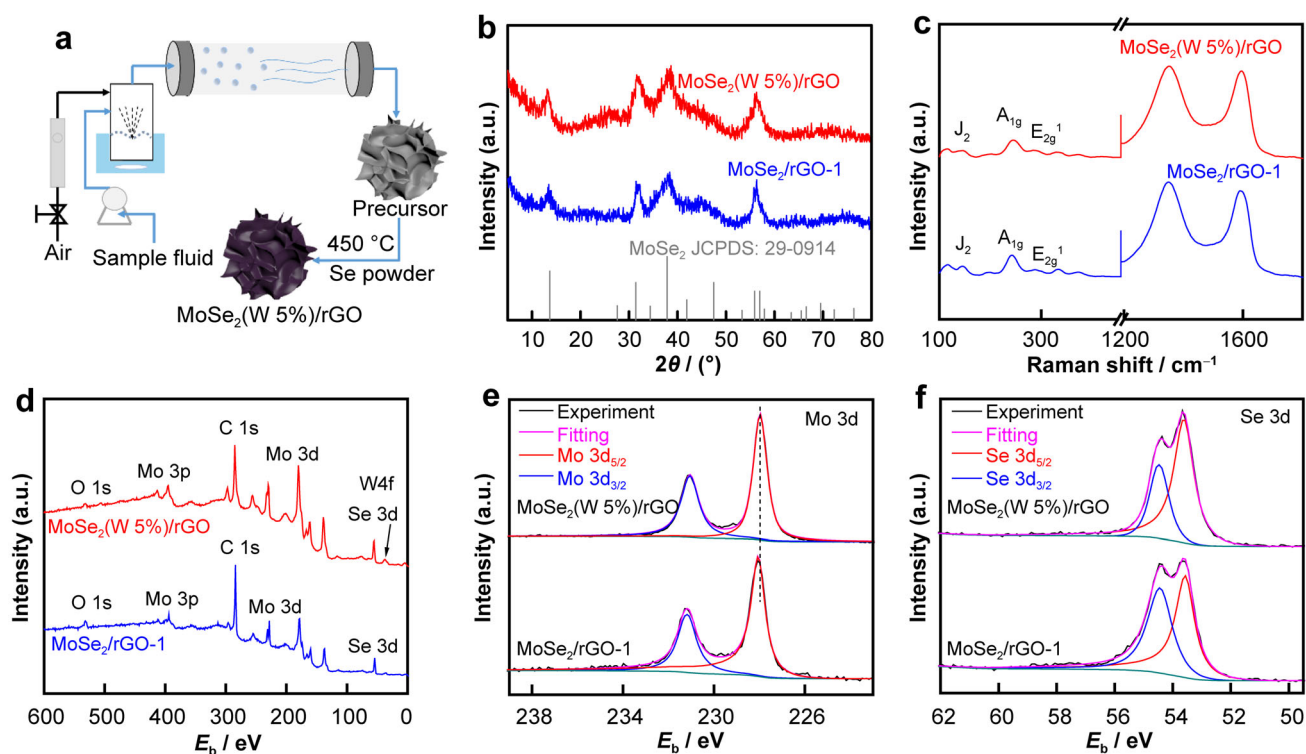
Fig. 1 **a** Schematic illustration for synthesis of MoSe₂(W 5%)/rGO; **b** XRD patterns and **c** Raman spectra of MoSe₂/rGO-1 and MoSe₂(W 5%)/rGO; **d** XPS spectra of MoSe₂(W 5%)/rGO and MoSe₂/rGO-1; high-resolution spectra of **e** Mo 3d and **f** Se 3d for MoSe₂(W 5%)/rGO and MoSe₂/rGO-1

0.223 g ammonium tungstate (with a W-to-Mo atomic ratio of 0.05:1, resulting in a 5% W doping) were dissolved in the dispersion. The subsequent steps followed the procedure described for MoSe₂/rGO-1. The resulting composite material was designated as MoSe₂(W 5%)/rGO. By adjusting the amount of ammonium tungstate to 0.045 g and 0.446 g (corresponding to W doping levels of 1% and 10% atomic ratios, respectively), different products were obtained and identified as MoSe₂(W 1%)/rGO and MoSe₂(W 10%)/rGO, respectively.

3 Results and discussion

The paper-like microsphere composite material was successfully synthesized through a simple process of ultrasonic spray pyrolysis and subsequent selenization annealing (Fig. 1a). Ultrasonic spray generated small droplets that entered a high-temperature tubular furnace with the carrier gas. The solvent rapidly evaporated under the high temperature, leading to the removal of oxygen-containing groups from GO and the self-assembly of formative reduced graphene oxide (rGO) into paper-like microspheres. Meanwhile, ammonium molybdate decomposed in the mildly alkaline and reduced environment provided by

HMTA, resulting in the formation of molybdenum oxide, which mixed thoroughly with the rGO paper-like microspheres. Subsequent selenidation produced MoSe₂, and due to the interaction between molybdenum species and rGO, the material retained the mesoscopic morphology of the initial spray-formed paper-like microspheres, while the layer number of MoSe₂ was constrained by rGO. The addition of a small amount of ammonium tungstate allowed for the synthesis of W-doped MoSe₂/rGO composite materials.

Figures 1b and S1a illustrate X-ray diffraction (XRD) patterns of samples. The peaks observed at $2\theta = 13.7°$, $31.4°$, $37.8°$ and $56.9°$ correspond to the (002), (100), (103) and (008) crystal planes of the 2H phase MoSe₂ (JCPDS No. 29-0914), respectively [40, 41], confirming the presence of the 2H phase MoSe₂ structure. Among all the samples, the characteristic diffraction peak at $2\theta = 31.4°$ exhibits significant intensity, comparable to the intensity of the maximum diffraction peak located at $2\theta = 37.8°$ in the standard card. This may be attributed to the intertwining of MoSe₂ and rGO within the composite, resulting in an altered crystal plane exposure of MoSe₂ in the composite material compared to the bulk MoSe₂. Additionally, broad and weak characteristic diffraction peaks around 26° correspond to the (002) plane of graphitic carbon in the

materials. This weak intensity can be attributed to the short pyrolysis time and the entangled composite structure of layered $MoSe_2$ and rGO, which hinders the graphitization of rGO. To elucidate the formation process of $MoSe_2$, XRD analysis was performed on the spray pyrolysis-derived precursor. From Fig. S1b, the diffraction peaks of P-$MoSe_2$ coincide with MoO_2 and MoO_3, indicating that ammonium molybdate decomposes into MoO_x in a weakly alkaline and reductive environment provided by HMTA. XRD patterns of the P-$MoSe_2$/rGO-1 and P-$MoSe_2$(W 5%)/rGO, as shown in Fig. S1c, only exhibit characteristic peaks of carbon, possibly due to the presence of rGO, which influences the growth of MoO_x crystals. The interaction between heterogeneous materials restricts the crystallinity of the materials, resulting in a decrease in the corresponding diffraction peak intensities [42]. These results demonstrate the successful synthesis of $MoSe_2$ and carbon composite materials through the proposed process.

Figure 1c presents the Raman spectra of the $MoSe_2$/rGO-1 and $MoSe_2$(W 5%)/rGO, which further confirms the presence of $MoSe_2$ and carbon materials in the composites. The two distinct peaks of the D and G bands for carbon, observed at ~ 1350 and ~ 1590 cm^{-1}, respectively, indicate the presence of carbon layer defects and in-plane vibrations of carbon atoms with sp^2 hybridization [36, 41]. It is observed that the peak intensity of the D band is stronger than that of the G band in all samples, suggesting that the carbon material and $MoSe_2$ composite create numerous structural defect sites, which are beneficial for the adsorption of Li^+ during energy storage. Additionally, the Raman spectra show peaks at 148, 238 and 282 cm^{-1}, corresponding to the J_2 phonon mode, in-plane A_{1g} and out-of-plane E_{2g}^1 vibration modes of $MoSe_2$, respectively [43]. The J_2 phonon mode represents the 1T phase of $MoSe_2$, while the in-plane A_{1g} and out-of-plane E_{2g}^1 vibration modes are associated with the 2H phase of $MoSe_2$ [44, 45]. The 2H phase of $MoSe_2$ is the most stable structure and exhibits semiconductor behavior, while the 1T phase has metallic properties but is less stable [46]. It is observed that the intensity of A_{1g} peak is higher than that of J_2 peaks, indicating that the material is predominantly composed of the 2H phase of $MoSe_2$. Despite its structural stability, the electrical conductivity of the material must be improved. These findings are in agreement with XRD results.

XPS spectroscopy was used to investigate the surface chemical environment of the $MoSe_2$(W 5%)/rGO and $MoSe_2$/rGO-1 samples. The full measurement spectrum (Fig. 1d) revealed characteristic peaks of Mo 3d, Se 3d, C 1s and O 1s in both samples. However, the intensity of the W 4f characteristic peak in the $MoSe_2$(W 5%)/rGO sample is quite weak due to the low concentration of W and the fact that XPS is a surface analysis technique.

Deconvolution fitting of the Mo 3d, Se 3d and O 1s peaks (Figs. 1e, f and S2a) reveal that the Mo and Se in the material are only involved in Mo-Se chemical bonding [24, 36]. Notably, there is a slight negative shift in the binding energy of Mo 3d in $MoSe_2$(W 5%)/rGO, indicating an increased electron density in $MoSe_2$ due to W doping [47]. The two fitted peaks of the O 1s peak correspond to C–O–H (532.4 eV) and C=O (530.2 eV), indicating the presence of non-lattice oxygen in the sample, suggesting that all the MoO_x species in the precursor have been completely selenidated during the synthesis process [41]. Figure S2b presents XPS high-resolution spectrum of W 4f. Through deconvolution fitting, two peaks corresponding to $4f_{7/2}$ and $4f_{5/2}$ are obtained, confirming the presence of W^{4+} in the sample [48]. The binding energy of the fitted peaks exhibits a slight positive shift compared to other reports, indicating that W doping can provide electrons to $MoSe_2$, thereby increasing the electron density of $MoSe_2$. This strengthens the interaction between $MoSe_2$ and rGO, facilitating the formation of van der Waals heterostructures.

The morphology of the different samples was characterized using scanning electron microscopy (SEM). Figures 2a and S3a, b show SEM images of the precursor materials, P-$MoSe_2$/rGO, with different metal contents. It can be seen that due to the rapid evaporation of the solvent during pyrolysis, the GO in the droplets contracts autonomously, leading to the formation of precursor materials with a spherical shape at the mesoscale level, as depicted in the scheme of Fig. 1a. At this stage, GO is transformed into rGO by removing oxygen functional groups, and ammonium molybdate decomposes into MoO_x. Selenization then predominantly converts MoO_x into layered 2H-phase $MoSe_2$, which intertwines with rGO, resulting in the formation of a paper-like spherical structure in the mesoscale (Fig. 2b–d). The growth of $MoSe_2$ is restrained by rGO, leading to the preservation of the original microsphere form after selenization. This result, combined with the analysis of XRD and Raman tests, suggests a strong interaction between $MoSe_2$ and rGO. Moreover, with increasing carbon content, the size of the microspheres slightly increases, while the $MoSe_2$/rGO-0.5 sample with the lowest carbon content has some agglomeration. On the other hand, the $MoSe_2$-rGO mixture obtained by simple mixing and calcination does not have a microsphere morphology, but rather an unstructured mixture of aggregated layers (Fig. S3c).

Figures 2e–g shows high-resolution transmission electron microscopy (HRTEM) images of $MoSe_2$/rGO-1, which demonstrate the presence of numerous wrinkles in rGO, further confirming the composite of $MoSe_2$ and rGO. The lattice fringes corresponding to the (002) plane in $MoSe_2$, the c-axis basal plane, can be seen in Fig. 2g. It is
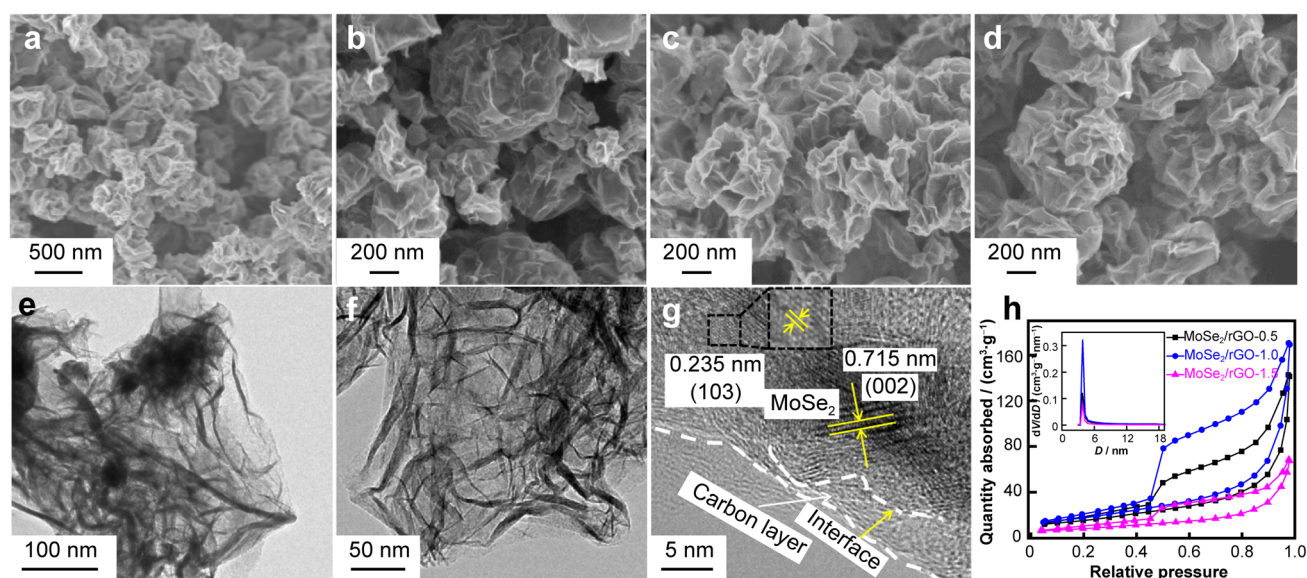
Fig. 2 SEM images of **a** P-MoSe$_2$/rGO-1, **b** MoSe$_2$/rGO-0.5, **c** MoSe$_2$/rGO-1 and **d** MoSe$_2$/rGO-1.5; **e–g** HRTEM images of MoSe$_2$/rGO-1; **h** N$_2$ adsorption/desorption isotherms and (inset) pore size distribution curves of MoSe$_2$/rGO samples

evident that the obtained MoSe$_2$ has a small number of layers (less than ten layers). Additionally, the interlayer spacing of the (002) plane is measured to be 0.715 nm, 11% wider than the standard value of 0.646 nm. This widening is likely due to the van der Waals heterostructure formed by the carbon layers and MoSe$_2$, which impedes the oriented growth of MoSe$_2$ crystals and causes the change in interlayer spacing [49, 50]. HRTEM images of MoSe$_2$/rGO-0.5 and MoSe$_2$/rGO-1.5 in Fig. S4 further confirm the formation of van der Waals heterostructures between MoSe$_2$ and rGO. Additionally, with an increase in carbon content, the interlayer distance of the (002) plane in MoSe$_2$ also increases, indicating that the alteration in interlayer spacing is a result of the interaction between MoSe$_2$ and rGO. These findings not only verify the microscopic interaction between MoSe$_2$ and rGO, but also suggest that the reduction in MoSe$_2$ layer numbers and the widening of MoSe$_2$ interlayer spacing, achieved through their interaction, could potentially improve the lithium storage performance of the composite.

Owing to the unique morphology of the materials in the form of paper-like microspheres, the nitrogen adsorption–desorption experiments were performed to determine the specific surface area and pore size distribution of the composite materials. Figure 2h presents the nitrogen adsorption–desorption isotherms and the corresponding pore size distribution curves of the three samples. All the three materials exhibited Type IV isotherms with H3 hysteresis loops, indicating their mesoporous nature with the dominant pore type being flat slit pores [51]. The specific surface areas of the samples by Brunauer–Emmett–Teller (BET) method were measured as 58.7, 122 and

103 m$^2 \cdot$g^{-1}, respectively. This result is consistent with the observations from SEM images, where MoSe$_2$/rGO-0.5 shows the accumulation of MoSe$_2$ due to its lower carbon content, while MoSe$_2$/rGO-1 and MoSe$_2$/rGO-1.5 have similar microsphere morphologies and comparable specific surface areas. However, MoSe$_2$/rGO-1 showed a more uniform mesoporous distribution and larger pore volume due to its moderate composition. The pore size distribution of the samples was concentrated around $\sim$ 3.8 nm, indicating that they are mesoporous materials. This result suggests that MoSe$_2$/rGO-1 has advantages in terms of electrolyte infiltration and diffusion, potentially leading to enhanced lithium storage performance. Additionally, using thermogravimetric analysis (TGA), the thermal weight loss curves of the samples in an air atmosphere were determined, as seen in Fig. S5. As the temperature rises, oxidation of MoSe$_2$ and carbon occurs leaving a residual mass fraction between 30% and 40% [38]. According to the TGA results, the mass fraction of selenides in MoSe$_2$(W 5%)/rGO is calculated to be 61.73%, while the content of carbonaceous materials is 38.27%.

Owing to the favorable microscopic and mesoscopic structural characteristics observed in the MoSe$_2$/rGO-1 sample, the doping of W element was carried out based on this optimal ratio. Figures 3a and S6a, b show SEM images of the MoSe$_2$/rGO with different doping W contents (1%, 5% and 10%). It can be observed that the mesoscopic morphology of the three samples, MoSe$_2$(W 1%)/rGO, MoSe$_2$(W 5%)/rGO and MoSe$_2$(W 10%)/rGO, still maintains a distinctive paper-like spherical structure. However, from a microscopic perspective, the doping of W may lead to increased disorder in the MoSe$_2$ crystal, thereby
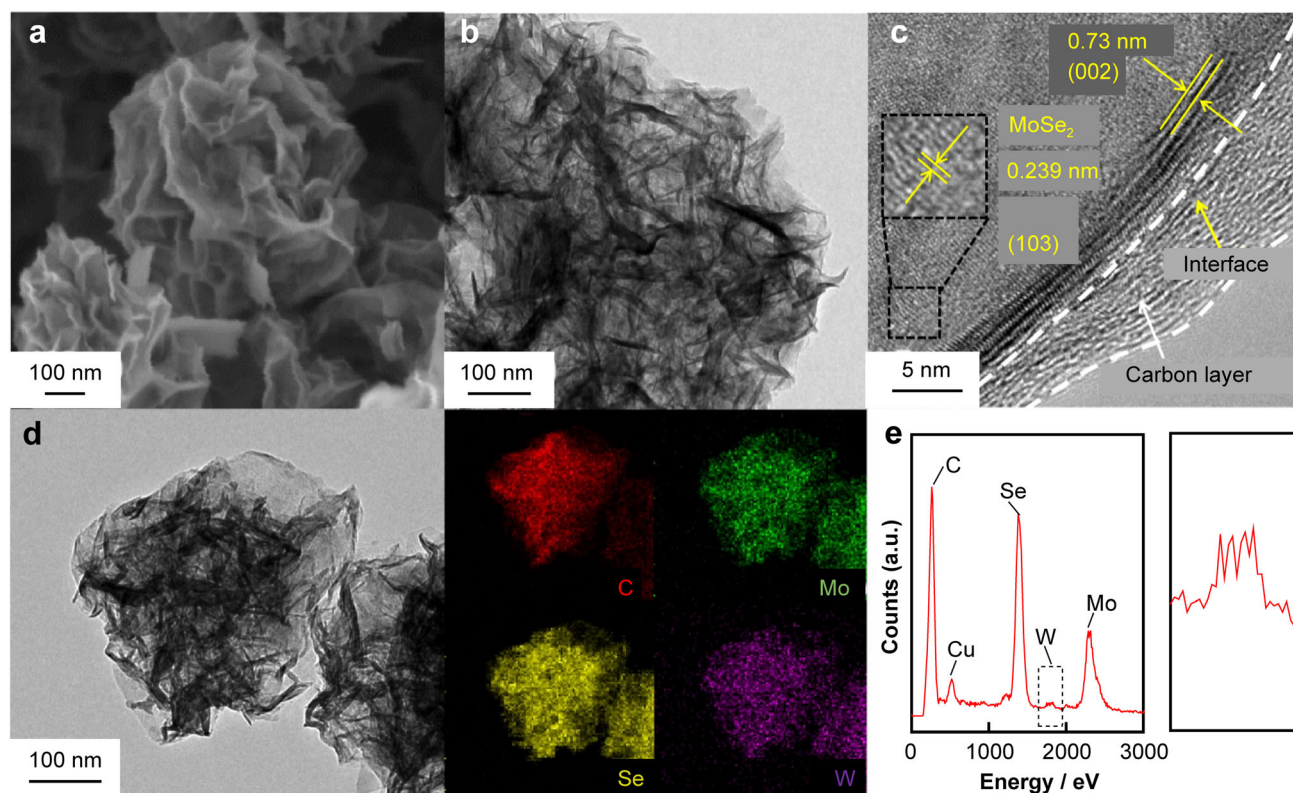
Fig. 3 **a** SEM image; **b** TEM image; **c** HRTEM image; **d** elemental mapping images and **e** EDS spectrum of MoSe$_2$(W 5%)/rGO

disrupting its crystal growth to some extent. This can weaken the interactions between the MoSe$_2$ layers, resulting in an expected MoSe$_2$ structure with an increased interlayer spacing and fewer layers [52]. TEM images in Figs. 3b and S6c, d confirm the above speculation. Compared to the undoped samples, the W-doped samples exhibit a more uniform dispersion of MoSe$_2$ and rGO. This is attributed to the easier formation of van der Waals heterostructures between the low-layer MoSe$_2$ and rGO. Figure 3c reveals that MoSe$_2$(W 5%)/rGO has fewer than five layers of MoSe$_2$, and the (002) crystal plane spacing is widened to 0.73 nm. Moreover, the carbon layer is aligned with MoSe$_2$, forming a beneficial van der Waals heterointerface. TEM mapping (Fig. 3d) reveals a uniform distribution of C, Mo, Se and W throughout the material. Additionally, the atomic ratios, obtained from the EDS analysis (Figs. 3e and S7), were calculated, showing that the actual molar fractions of W relative to the total amount of Mo and W in MoSe$_2$(W 1%)/rGO, MoSe$_2$(W 5%)/rGO and MoSe$_2$(W 10%)/rGO are 0.72%, 2.64% and 6.31%, respectively.

However, EDS is a semi-quantitative analytical method. In order to obtain accurate molar fractions of Mo and W in the sample, inductively coupled plasma optical emission spectroscopy (ICP-OES) was employed to analyze the elemental content in MoSe$_2$(W 5%)/rGO. The obtained

mass fractions of Mo and W were found to be 22.37% and 1.96%, respectively. Based on this, it can be calculated that W accounts for 4.39% of the total Mo and W substances in the composite material. Furthermore, calculations reveal that the mass fraction of selenides in the composite material is 62.83%, thereby confirming the accuracy of the previous TGA results.

Cyclic voltammetry (CV) technique was used to investigate the lithiation/delithiation processes of the materials. Figures 4a and S8a show CV curves of MoSe$_2$(W 5%)/rGO and MoSe$_2$/rGO-1, respectively, during the initial five charge/discharge cycles. The reduction peak at around 0.6 V in the first cathodic scan of MoSe$_2$/rGO-1 corresponds to the phase transition and lithium storage reaction of MoSe$_2$, where the material transforms from MoSe$_2$ to Li$_x$MoSe$_2$ and further decomposes into Mo and Li$_2$Se upon Li$^+$ insertion [53]. This process is accompanied by the transformation of MoSe$_2$ from the 2H phase to the 1T phase [54–56]. There is also a reduction peak at around 0.25 V, which is due to the formation of the solid electrolyte interface (SEI) [55]. After the first cycle, the reduction peak (around 1.7 V) and oxidation peak (around 2.4 V) in CV curves indicate the conversion reactions between Li$_2$Se and MoSe$_2$ [24]. The good overlap of CV curves after the first cycle demonstrates the excellent stability of material, which is attributed to the formation of van der Waals
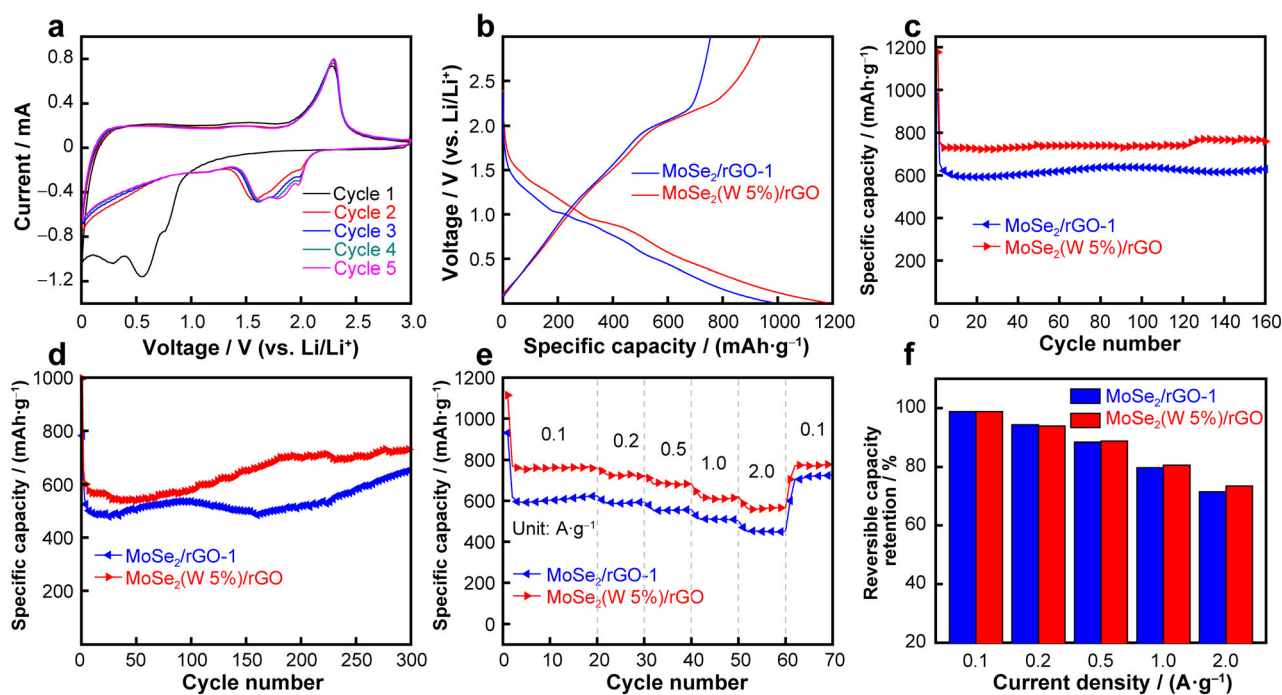
Fig.4 **a** CV curves of MoSe$_2$(W 5%)/rGO at 0.5 mV·s^{-1}; **b** the 1st GCD profiles of MoSe$_2$(W 5%)/rGO and MoSe$_2$/rGO-1 at 0.2 A·g^{-1}; cycling performance of MoSe$_2$(W 5%)/rGO and MoSe$_2$/rGO-1 at **c** 0.2 A·g^{-1} and **d** 1 A·g^{-1}; **e** rate performance and **f** corresponding bar diagram of capacity retention for MoSe$_2$(W 5%)/rGO and MoSe$_2$/rGO-1 at different current densities of 0.1 A·g^{-1}, 0.2 A·g^{-1}, 0.5 A·g^{-1}, 1 A·g^{-1} and 2 A·g^{-1}

heterointerfaces and the unique paper-like microsphere morphology. Compared to MoSe$_2$/rGO-1, MoSe$_2$(W 5%)/rGO exhibits an increased number of reduction peaks in CV curves, indicating enhanced redox reaction activity of the material [57]. This phenomenon confirms that doping W can adjust and enhance the intrinsic electronic structure of MoSe$_2$, consequently increasing the lithium storage performance of the material. Figure 4b illustrates the constant current charge–discharge profiles of MoSe$_2$/rGO-1 and MoSe$_2$(W 5%)/rGO, respectively, at a current density of 200 mA·g^{-1} for the 1st cycle. The initial discharge capacities of MoSe$_2$/rGO-1 and MoSe$_2$(W 5%)/rGO are 981.3 and 1176.9 mAh·g^{-1}, respectively. The initial charge capacity of the samples is lower than the discharge capacity, which can be attributed to the irreversible reactions that occur during the first discharge, such as the formation of SEI. The 1st cycle charge capacity of MoSe$_2$/rGO-1 and MoSe$_2$(W 5%)/rGO is 755.4 and 937.8 mAh·g^{-1}, respectively, corresponding to irreversible losses of 23.02% and 20.32%.

To compare the differences in lithium storage performance, cyclic stability tests were conducted on the samples at different current densities. Figure 4c shows the results of MoSe$_2$/rGO-1 and MoSe$_2$(W 5%)/rGO at a current density of 200 mA·g^{-1}. It can be observed that MoSe$_2$/rGO-1 exhibits excellent cyclic stability, with a reversible specific capacity of around 600 mAh·g^{-1}. On the other hand, MoSe$_2$(W 5%)/rGO, benefiting from its superior micro and mesostructure, maintains a reversible specific capacity of around 750 mAh·g^{-1}. Based on the mass fractions of individual components and theoretical specific capacity in MoSe$_2$(W 5%)/rGO, it can be calculated that the theoretical specific capacity of this composite material is 545 mAh·g^{-1}. The capacity exceeding the theoretical value originates from the excellent structure of the composite material. From a mesoscale perspective, the unique morphology of paper-like microspheres in the material can accommodate the volume expansion during lithium storage. From a microscale perspective, the doping of W elements further improves the intrinsic electronic structure of MoSe$_2$, widens the interlayer spacing, and reduces the number of layers, facilitating the formation of van der Waals heterostructures with rGO. This promotes the adsorption of Li$^+$ on the surface of material and diffusion within the bulk. These advantages are also reflected in the rate performance test results. The long-term cycling stability of the samples at a current density of 1 A·g^{-1} is shown in Figs. 4d and S8b–d. It can be observed that the MoSe$_2$-rGO mixture obtained by directly mixing and calcining MoSe$_2$ with GO exhibits a capacity of only 284 mAh·g^{-1} after 300 cycles. The stability is attributed to the protective effect of rGO, however, due to the lack of a well-formed van der Waals heterostructure between MoSe$_2$ and rGO, the lithium storage capacity of MoSe$_2$-rGO

Table 1 Comparison of lithium storage cycle performance between this work and some other works reported previously

Samples	Current density / ($mA \cdot g^{-1}$)	Cycle number	Remaining capacity / ($mAh \cdot g^{-1}$)	Refs.
$MoSe_2(W5\%)$/rGO	1000	300	732.9	This work
e-$MoSe_2$	0.2C	100	630.9	[58]
$MoSe_2$@C	500	300	711	[59]
Mo-$MoSe_2$	0.2C	50	550	[43]
PVP/SiOC/$MoSe_2$	50	100	450	[60]
$MoSe_2$@CC	5000	1200	638	[61]
$MoSe_2 \perp$SFAC	100	50	501.3	[62]
$MoSe_2$/graphite	100	100	787.3	[63]
$MoSe_2$/MoO_2	100	100	1042	[64]

mixture is not high. On the other hand, $MoSe_2$/rGO-1 maintains a capacity of 655 mAh·g^{-1} after 300 cycles at a current density of 1 A·g^{-1}, while $MoSe_2$(W 5%)/rGO has a high capacity of 732.9 mAh·g^{-1}. Besides, compared to other reported $MoSe_2$-based lithium-ion battery anodes, $MoSe_2$(W 5%)/rGO exhibits superior performance, as illustrated in Table 1 [43, 58–64].

Notably, both of these materials show an increase in capacity with cycling and surpass the theoretical capacity. This is thought to be due to the continuous refinement of $MoSe_2$ during charge and discharge cycles while keeping it within the microspheres, thus increasing the number of effective active sites [65]. To ascertain the microstructural changes of the materials after charge–discharge cycling, SEM and TEM were conducted on sample cycled for 50 cycles at a current density of 1 A·g^{-1}. As shown in Fig. S9a, the material retains its microsphere morphology. However, under the influence of phase transition stress, the paper-like morphology of the material is disrupted and gradually transforms into microspheres composed of two-dimensional nanosheets, as depicted in Fig. S9b. Figure S9c, d presents TEM images of the material after cycling, demonstrating that $MoSe_2$ remains coupled with rGO, with the refined $MoSe_2$ retained within the microsphere structure, contributing to the continuous increase in specific capacity.

Figure 4e shows that at different current densities of 0.1, 0.2, 0.5, 1 and 2 A·g^{-1}, $MoSe_2$(W 5%)/rGO demonstrates superior rate performance, with a discharge specific capacity of around 560 mAh·g^{-1} at 2 A·g^{-1}, and a capacity of around 770 mAh·g^{-1} when the current density is returned to 100 mA·g^{-1}. The reversible capacity retention of $MoSe_2$/rGO-1 and $MoSe_2$(W 5%)/rGO at different rates is compared in Fig. 4f. It can be observed that as the current density increases, the reversible capacity retention

of the materials decreases due to polarization. However, the superior microstructure of $MoSe_2$(W 5%)/rGO facilitates the rapid insertion and extraction of Li^+, allowing for a higher level of reversible capacity retention than that of $MoSe_2$/rGO-1. At a high current density of 2 A·g^{-1}, $MoSe_2$(W 5%)/rGO has a reversible capacity retention of 73.8%, while $MoSe_2$/rGO-1 only retains 71.5%. The well-formed van der Waals heterostructure of $MoSe_2$(W 5%)/rGO allows the material to have better Li^+ adsorption capability, where Li^+ is adsorbed at the surfaces/interfaces of the materials, providing rapid lithium storage ability [66]. Therefore, $MoSe_2$(W 5%)/rGO, which has the optimal microstructure and mesostructure, has the best lithium storage performance, surpassing $MoSe_2$/rGO-1 and other composite materials.

In order to study the kinetic differences between $MoSe_2$(W 5%)/rGO and $MoSe_2$/rGO-1 for lithium storage, CV curves of the two materials at different scanning rates of 0.2–1 mV·s^{-1} were tested, as shown in Figs. 5a and S10a. Both the cathodic and anodic peak intensities of both $MoSe_2$/rGO-1 and $MoSe_2$(W 5%)/rGO increase with the scanning rate, and the peak positions of both cathodic and anodic peaks shift with the scanning rate due to electrochemical polarization. However, $MoSe_2$(W 5%)/rGO exhibits smaller changes in peak amplitudes than $MoSe_2$/rGO-1, indicating better reversibility of the electrochemical reactions [67]. This suggests that $MoSe_2$(W 5%)/rGO has remarkable electrochemical kinetics, facilitating the rapid insertion and extraction of Li^+ during the charge–discharge process. The contribution of capacitance control and diffusion control to the capacity of simple can be determined using the formula $i = k_1 v + k_2 v^{1/2}$, where $k_1 v$ represents capacitance control and $k_2 v^{1/2}$ represents diffusion control [68]. Figures 5b and S10b show the capacitance contribution to the lithium storage capacity of $MoSe_2$(W 5%)/rGO and $MoSe_2$/rGO-1, respectively, at a scanning rate of 1.0 mV·s^{-1}. The capacitance contribution is indicated by the shaded area. The calculations reveal that the capacitance contribution to the lithium storage capacity of $MoSe_2$(W 5%)/rGO is 60.2%, while for $MoSe_2$/rGO-1, it is 51.6%. The high capacitance contribution in $MoSe_2$(W 5%)/rGO confirms its high rate performance from a kinetic perspective, which is closely related to its superior van der Waals heterostructure and the favorable adsorption of lithium ions at the surface/interface of material [69].

The intensity of the peak current in CV curve is influenced by the scanning rate and the diffusion rate of Li^+ ions (D_{Li^+}). As depicted in Fig. 5c, both the cathodic and anodic peak currents of the two samples exhibit a linear correlation with the square root of the scanning rate ($v^{1/2}$). Consequently, the Li^+ diffusion within the materials can be determined by employing the classical Randles–Sevchik equation [70]:
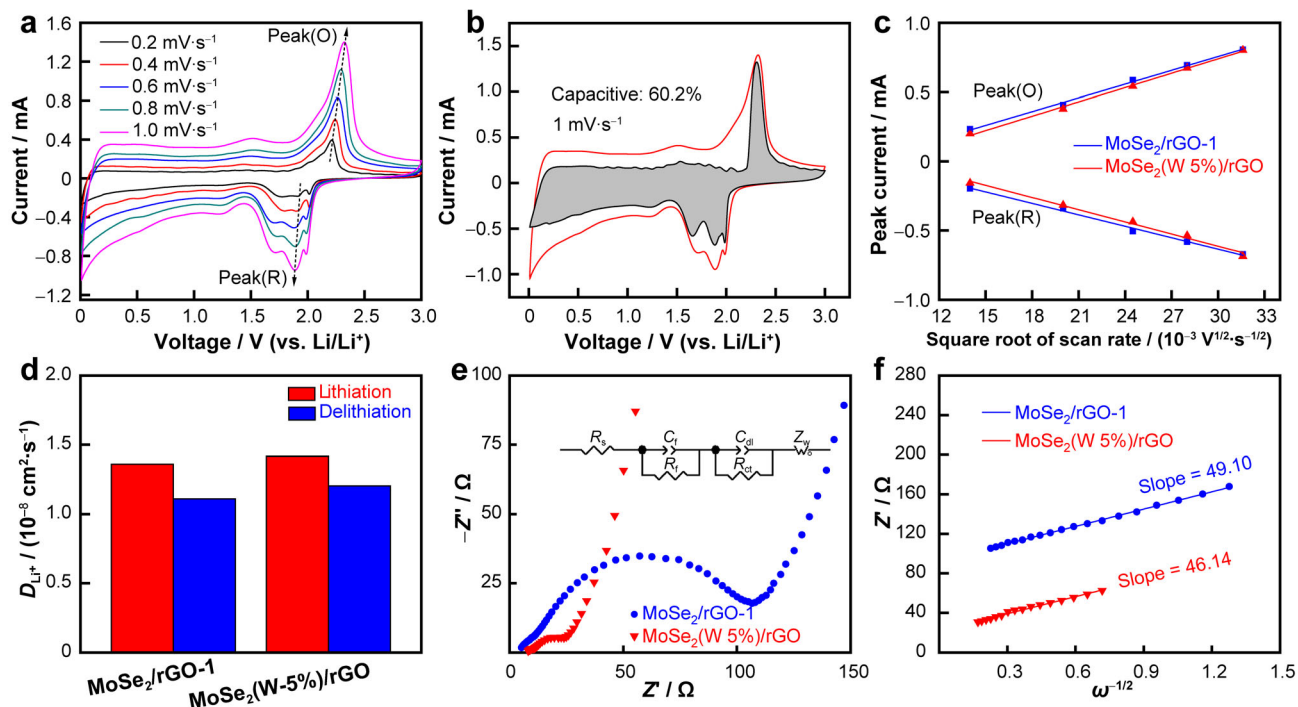
Fig. 5 **a** CV curves of MoSe₂(W 5%)/rGO at various scan rates; **b** separation of capacitive current at a scan rate of 1 mV·s⁻¹ with capacitive fraction shown by shaded region; **c** relationship of peak current (i_p) and square root of scan rate ($v^{1/2}$); **d** apparent diffusion rate of Li⁺ for MoSe₂(W 5%)/rGO and MoSe₂/rGO-1; **e** EIS of MoSe₂(W 5%)/rGO and MoSe₂/rGO-1 and (inset) equivalent circuits; **f** corresponding linear fitting of Warburg impedance

$$i_p = (2.69 \times 10^5)n^{3/2}SD^{1/2}Cv^{1/2} \tag{1}$$

where n is the charge-transfer number, i_p is the peak current (A), S is the electrode area, D is the diffusion coefficient of Li⁺ (cm²·s⁻¹), C is the concentration of Li⁺ and v is the scan rate (V·s⁻¹).

Based on the fitting analysis of Fig. 5c, the calculated values of apparent D_{Li^+} at the cathodic and anodic peaks for MoSe₂(W 5%)/rGO and MoSe₂/rGO-1 are presented in the bar chart of Fig. 5d. The apparent D_{Li^+} values for lithium insertion and extraction in MoSe₂/rGO-1 were calculated to be 1.36×10^{-8} and 1.11×10^{-8} cm²·s⁻¹, respectively. On the other hand, MoSe₂(W 5%)/rGO showed higher D_{Li^+} values of 1.42×10^{-8} cm²·s⁻¹ for insertion and 1.20×10^{-8} cm²·s⁻¹ for extraction. This indicates that widening of the interlayer spacing in MoSe₂ as well as the improved van der Waals heterostructure due to W doping leads to faster lithium insertion and extraction, resulting in superior lithium storage performance compared to MoSe₂/rGO-1.

Figures 5e and S11a display the Nyquist plots obtained from the alternative current (AC) impedance measurements of the composite materials after 10 charge–discharge cycles. The inset in Fig. 5e illustrates the impedance equivalent circuit, wherein R_s stands for the electrolyte resistance, which is equivalent to the intercept on the x-axis of the high-frequency region arc [71]; R_f and R_{ct} represent the charge-transfer impedance between the electrolyte and the SEI, and the SEI and the internal electrode interface, respectively, corresponding to the diameter of the high-frequency region arc [72]; Z_w is the Warburg impedance connected to Li⁺ diffusion in the material, that is equal to the linear part in the low-frequency region [36]. It can be clearly observed that, after 10 charge–discharge cycles, MoSe₂(W 5%)/rGO exhibits a lower interfacial resistance. Additionally, an analysis of Z_w was performed by linearly fitting the impedance Z' in the low-frequency region with the reciprocal square root of the angular frequency ($\omega^{-1/2}$). The obtained slope σ represents the Warburg factor, which is correlated with the lithium-ion diffusion coefficient D_{Li^+}. The corresponding formulas are as follows [20]:

$$Z' = R_{ct} + R_s + \sigma\omega^{-1/2} \tag{2}$$

$$D = R^2T^2/(2A^2n^4F^4C_{Li}\sigma^2) \tag{3}$$

where R is the gas constant (8.314 J·K⁻¹), T is the absolute temperature (298 K), A is the surface area of the electrode, n is the electrons number per molecule in intercalation process, F is the Faraday constant (96,485 C·mol⁻¹), C_{Li} is the Li⁺ molar concentration in electrode, ω is the angular frequency and σ is the Warburg factor related with Z'.
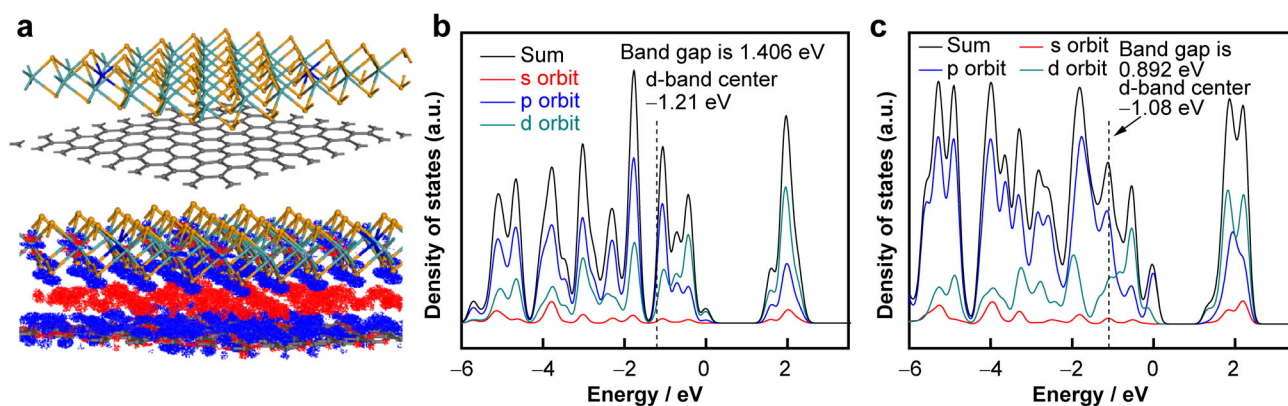
Fig. 6 **a** Model of $MoSe_2$(W 5%)/rGO and corresponding electron density difference result of $MoSe_2$(W 5%)/rGO; DOS results of **b** $MoSe_2$/rGO and **c** $MoSe_2$(W 5%)/rGO

The fitting results in Figs. 5f and S11b show that $MoSe_2$(W 5%)/rGO has a σ value of 46.14, lower than the other samples, thus demonstrating its superior lithium-ion diffusion performance, as previously found.

In order to gain a deeper understanding of the effect of W doping on the electrochemical performance of materials, DFT (details in Supplementary Information) was used to study the differences between $MoSe_2$(W 5%)/rGO and $MoSe_2$/rGO. Figure S12a, b depicts the models of single-layer graphene and single-layer $MoSe_2$, respectively. By combining these two, the model for the $MoSe_2$/rGO heterointerface is obtained. To create the $MoSe_2$(W 5%)/rGO heterointerface, Mo atoms are replaced with W atoms in situ, with W atoms accounting for 5% of the total atomic content of W and Mo. Figures 6a and S12c show the electron density difference results of $MoSe_2$(W 5%)/rGO and $MoSe_2$/rGO, respectively. The red and blue regions signify electron gain and loss, respectively. It can be observed that the charge transfer between $MoSe_2$ and graphene is enhanced after W doping, which is consistent with the experimental results such as XPS. W doping optimizes the van der Waals heterostructure, strengthens the interaction between $MoSe_2$ and rGO, and enhances the interface reactivity [73–75]. Additionally, the calculated density of states (DOS) result (Fig. 6b, c) indicates that the band gap of $MoSe_2$/rGO is 1.406 eV, while that of $MoSe_2$(W 5%)/rGO is 0.892 eV. This confirms that W doping increases the intrinsic conductivity of $MoSe_2$ [73, 76]. Furthermore, W doping shifts the center of the d band in the material from -1.21 eV in $MoSe_2$/rGO to -1.08 eV in $MoSe_2$(W 5%)/rGO, which is beneficial for Li^+ adsorption [77]. Thus, DFT calculation reveals that W doping can optimize the microstructure of material and enhance its lithium storage performance.

4 Conclusion

In summary, a W-doped $MoSe_2$ composite rGO paper-like microsphere material was prepared via a simple ultrasonic spray pyrolysis process. The material has been optimized at both the microstructure and mesostructure. On the microstructure, the material has an increased interlayer distance and fewer layers of $MoSe_2$, plus W doping promotes the interaction between $MoSe_2$ and rGO, creating a more efficient van der Waals heterostructure. This facilitates the diffusion of Li^+ in the material and its adsorption on the surface/interface. On the mesostructure, the paper-like microspheres provide additional space for volume expansion. These structural improvements result in excellent lithium storage capacity, cycle stability, rate performance and kinetics. The reversible specific capacity of the material can still remain 732.9 $mAh \cdot g^{-1}$, at the current density of 1 $A \cdot g^{-1}$ after 300 cycles. Furthermore, DFT calculations have revealed the role of W doping in optimizing the lithium storage performance of $MoSe_2$/rGO. The preparation and modification strategies employed in this study can provide insights and ideas for the design and fabrication of other lithium storage composite materials.

Declarations

Conflict of interests The authors declare that they have no conflict of interest.

Open Access This article is licensed under a Creative Commons Attribution 4.0 International License, which permits use, sharing, adaptation, distribution and reproduction in any medium or format, as long as you give appropriate credit to the original author(s) and the source, provide a link to the Creative Commons licence, and indicate if changes were made. The images or other third party material in this article are included in the article's Creative Commons licence, unless indicated otherwise in a credit line to the material. If material is not included in the article's Creative Commons licence and your intended use is not permitted by statutory regulation or exceeds the permitted use, you will need to obtain permission directly from the copyright holder. To view a copy of this licence, visit http://creativecommons.org/licenses/by/4.0/.

References

[1] Zuo JH, Zhai PB, He QQ, Wang L, Chen Q, Gu XK, Yang ZL, Gong YJ. In-situ constructed three-dimensional MoS₂–MoN heterostructure as the cathode of lithium–sulfur battery. Rare Met. 2022;41(5):1743. https://doi.org/10.1007/s12598-021-01910-1.

[2] Yin H, Luo J, Li HY, Liu A, Li GY, Zhu YC, Huang JL, Cao ML, Hou ZH. Point-cavity-like carbon layer coated SnS nanotubes with improved energy storage capacity for lithium/sodium ion batteries. J Energy Storage. 2023;65:107354. https://doi.org/10.1016/j.est.2023.107354.

[3] Chen LJ, Liu TT, Liu SM, Cai S, Zou XX, Jiang JW, Mei ZY, Zhao GF, Yang XF, Guo H. S vacant CuIn₅S₈ confined in a few-layer MoSe₂ with interlayer-expanded hollow heterostructures boost photocatalytic CO₂ reduction. Rare Met. 2022;41(1):144. https://doi.org/10.1007/s12598-021-01809-x.

[4] Yin H, Li HY, Yu XX, Cao ML. Design of Sb₂Te₃ nanoblades serialized by Te nanowires for a low-temperature near-infrared photodetector. Front Chem. 2022;10:1060523. https://doi.org/10.3389/fchem.2022.1060523.

[5] Li Z, Wang W, Zhou MJ, He BH, Ren WQ, Chen L, Xu WY, Hou ZH, Chen YY. In-situ self-templated preparation of porous core–shell Fe₁₋ₓS@N, S Co-doped carbon architecture for highly efficient oxygen reduction reaction. J Energy Chem. 2021;54:310. https://doi.org/10.1016/j.jechem.2020.06.010.

[6] Li HY, Luo J, Han DY, Liu A, Zhou M, Huang JL, Zhu YC, Hou ZH, Yin H. Layer-by-layer hetero-carbon modifying ZnS nanocubes anode with improved long-term life for sodium-ion batteries. Ceram Int. 2023;49(11):18421. https://doi.org/10.1016/j.ceramint.2023.02.214.

[7] Yin H, Han DY, Yu XX, Cao ML, Hou ZH, Li C, Zhu MQ. Recent advances in electrospun metal chalcogenide anodes for lithium-ion and sodium-ion batteries. ACS Appl Energy Mater. 2023;6(3):1155. https://doi.org/10.1021/acsaem.2c03309.

[8] Lin XP, Xue FF, Zhang ZG, Li QH. Sb nanoparticles encapsulated in N-doped carbon nanotubes as freestanding anodes for high-performance lithium and potassium ion batteries. Rare Met. 2023;42(2):449. https://doi.org/10.1007/s12598-022-02143-6.

[9] Liu YP, Xu CX, Ren WQ, Hu LY, Fu WB, Wang W, Yin H, He BH, Hou ZH, Chen L. Self-template synthesis of peapod-like MnO@N-doped hollow carbon nanotubes as an advanced anode for lithium-ion batteries. Rare Met. 2023;42(3):929. https://doi.org/10.1007/s12598-022-02203-x.

[10] Wang W, Wang HT, Wu ZX, Yu Y, Asif M, Wang ZY, Qiu XY, Liu HF. Co/MnO/NC hybrid derived from N-methyl-D-glucamine as efficient bifunctional oxygen electrocatalysts. Electrochim Acta. 2018;281:486. https://doi.org/10.1016/j.electacta.2018.05.207.

[11] Wang W, Wang HT, Yu Y, Wu ZX, Asif M, Liu HF. Metallic cobalt modified MnO–C nanocrystalline composites as an efficient bifunctional oxygen electrocatalyst. Catal Sci Technol. 2018;8(2):480. https://doi.org/10.1039/C7CY01957B.

[12] Lin HJ, Lu YS, Zhang LT, Liu HZ, Edalati K, Révész Á. Recent advances in metastable alloys for hydrogen storage: a review. Rare Met. 2022;41(6):1797. https://doi.org/10.1007/s12598-021-01917-8.

[13] Li GY, Long YT, Li Z, Li SP, Zheng Y, He BH, Zhou M, Hu ZQ, Zhou MJ, Hou ZH. Reducing the charging voltage of a Zn-air battery to 1.6 V enabled by redox radical-mediated biomass oxidation. ACS Sustainable Chem Eng. 2023;11:8642. https://doi.org/10.1021/acssuschemeng.3c01799.

[14] Wang LF, Yang RX, Fu JZ, Cao YY, Ding RF, Xu XH. Vertically aligned W(Mo)S₂/NW(Mo)C-based light-assisted electrocatalysis for hydrogen evolution in acidic solutions. Rare Met. 2023;42(5):1535. https://doi.org/10.1007/s12598-022-02250-4.

[15] Zhang YX, Zhang L, Lv Ta, Chu PK, Huo KF. Two-dimensional transition metal chalcogenides for alkali metal ions storage. Chemsuschem. 2020;13(6):1114. https://doi.org/10.1002/cssc.201903245.

[16] He C, Zhang J, Zhang W, Li T. GeSe/BP van der Waals heterostructures as promising anode materials for potassium-ion batteries. J Phys Chem C. 2019;123(9):5157. https://doi.org/10.1021/acs.jpcc.8b08909.

[17] Mao Q, Liu J, Cao Q, Yang D, Zhong J, Sun G, Zheng J, Kuang L, Guo B, Liu Q. Porous carbon nanorods decorated with graphitic carbon bubbles encapsulated NiSe nanoparticles as an efficient microwave absorber. Ceram Int. 2020;46(9):13752. https://doi.org/10.1016/j.ceramint.2020.02.164.

[18] Nithya V. Recent advances in CoSe₂ electrocatalysts for hydrogen evolution reaction. Int J Hydrogen Energ. 2021;46(73):36080. https://doi.org/10.1016/j.ijhydene.2021.08.157.

[19] Zhang F, Shen Y, Shao M, Zhang YC, Zheng B, Wu JS, Zhang WN, Zhu AP, Huo FW, Li S. SnSe₂ nanoparticles chemically embedded in a carbon shell for high-rate sodium-ion storage. ACS Appl Mater Interfaces. 2019;12(2):2346. https://doi.org/10.1021/acsami.9b16659.

[20] Zhou QP, Wang DW, Lian Y, Hou SY, Ban CL, Wang ZF, Zhao J, Zhang HH. Rechargeable aluminum-ion battery with sheet-like MoSe₂@C nanocomposites cathode. Electrochim Acta. 2020;354:136677. https://doi.org/10.1016/j.electacta.2020.136677.

[21] Shu HB, Zhou D, Li F, Cao D, Chen XS. Defect engineering in MoSe₂ for the hydrogen evolution reaction: from point defects to edges. ACS Appl Mater Interfaces. 2017;9(49):42688. https://doi.org/10.1021/acsami.7b12478.

[22] Eftekhari A. Molybdenum diselenide (MoSe₂) for energy storage, catalysis, and optoelectronics. Appl Mater Today. 2017;8:1. https://doi.org/10.1016/j.apmt.2017.01.006.

[23] Mahankali K, Gottumukkala SV, Masurkar N, Thangavel NK, Jayan R, Sawas A, Nagarajan S, Islam MM, Arava LMR. Unveiling the electrocatalytic activity of 1T′-MoSe₂ on lithium-polysulfide conversion reactions. ACS Appl Mater Interfaces. 2022;14(21):24486. https://doi.org/10.1021/acsami.2c05508.

[24] Liu YL, Wang NN, Zhao XH, Fang ZW, Zhang X, Liu YY, Bai ZC, Dou SX, Yu GH. Hierarchical nanoarchitectured hybrid electrodes based on ultrathin MoSe₂ nanosheets on 3D ordered macroporous carbon frameworks for high-performance sodium-ion batteries. J Mater Chem A. 2020;8(5):2843. https://doi.org/10.1039/C9TA13377A.

[25] Wu X, Wang YH, Li PL, Xiong ZZ. Research status of MoSe$_2$ and its composites: a review. Superlattices Microstruct. 2020; 139:106388. https://doi.org/10.1016/j.spmi.2020.106388.

[26] Lei T, Gu M, Fu H, Wang J, Wang L, Zhou J, Liu H, Lu B. Bond modulation of MoSe$_{2+x}$ driving combined intercalation and conversion reactions for high-performance K cathodes. Chem Sci. 2023;14(10):2528. https://doi.org/10.1039/D2SC07121E.

[27] Liu L, Xu J, Sun J, He S, Wang K, Chen Y, Dou S, Du Z, Du H, Ai W. A stable and ultrafast K ion storage anode based on phase-engineered MoSe$_2$. Chem Commun. 2021;57(32):3885. https://doi.org/10.1039/D1CC00341K.

[28] Guo JZ, Sun XH, Shen KE, Li X, Zhang N, Hou TY, Fan AR, Jin SB, Hu XD, Li TT. Controllable synthesis of tunable few-layered MoS$_2$ chemically bonding with in situ conversion nitrogen-doped carbon for ultrafast reversible sodium and potassium storage. Chem Eng J. 2020;393:124703. https://doi.org/10.1016/j.cej.2020.124703.

[29] Zhang YQ, Tao HC, Li T, Du SL, Li JH, Zhang YK, Yang XL. Vertically oxygen-incorporated MoS$_2$ nanosheets coated on carbon fibers for sodium-ion batteries. ACS Appl Mater Interfaces. 2018;10(41):35206. https://doi.org/10.1021/acsami.8b12079.

[30] Yao ZJ, Yu CY, Dai HH, Zhou JY, Liu X, Sun GZ. Hybrid fibers assembled from MoSe$_2$/graphene heterostructures endow improved supercapacitive performance. Carbon. 2022;187:165. https://doi.org/10.1016/j.carbon.2021.11.009.

[31] Zhang JY, Liu YC, Sun CQ, Xi PX, Peng SL, Gao DQ, Xue DS. Accelerated hydrogen evolution reaction in CoS$_2$ by transition-metal doping. ACS Energy Lett. 2018;3(4):779. https://doi.org/10.1021/acsenergylett.8b00066.

[32] Wang TT, Guo XS, Zhang JY, Xiao W, Xi PX, Peng SL, Gao DQ. Electronic structure modulation of NiS$_2$ by transition metal doping for accelerating the hydrogen evolution reaction. J Mater Chem A. 2019;7(9):4971. https://doi.org/10.1039/C8TA11286J.

[33] Sun C, Wang Y, McMurtrey MD, Jerred ND, Liou F, Li J. Additive manufacturing for energy: a review. Appl Energ. 2021; 282:116041. https://doi.org/10.1016/j.apenergy.2020.116041.

[34] Wang P, Xi B, Huang M, Chen W, Feng J, Xiong S. Emerging catalysts to promote kinetics of lithium–sulfur batteries. Adv Energy Mater. 2021;11(7):2002893. https://doi.org/10.1002/aenm.202002893.

[35] Tang X, Liu D, Wang YJ, Cui L, Ignaszak A, Yu Y, Zhang J. Research advances in biomass-derived nanostructured carbons and their composite materials for electrochemical energy technologies. Prog Mater Sci. 2021;118:100770. https://doi.org/10.1016/j.pmatsci.2020.100770.

[36] Ge P, Hou HS, Banks CE, Foster CW, Li SJ, Zhang Y, He JY, Zhang CY, Ji XB. Binding MoSe$_2$ with carbon constrained in carbonous nanosphere towards high-capacity and ultrafast Li/Na-ion storage. Energy Storage Mater. 2018;12:310. https://doi.org/10.1016/j.ensm.2018.02.012.

[37] Hu R, Sha D, Cao X, Lu C, Wei Y, Pan L, Sun Z. Anchoring metal-organic framework-derived ZnTe@C onto elastic Ti$_3$C$_2$T$_x$ MXene with 0D/2D dual confinement for ultrastable potassium-ion storage. Adv Energy Mater. 2022;12(47):2203118. https://doi.org/10.1002/aenm.202203118.

[38] Wu LD, Tan PF, Liu Y, Xiong X, Pan J. Effects of Carbon Content on the Lithium-Storage Properties of MoSe$_2$-C Nanocomposites. ChemistrySelect. 2017;2(26):8101. https://doi.org/10.1002/slct.201700818.

[39] Sha D, Lu C, He W, Ding J, Zhang H, Bao Z, Cao X, Fan J, Dou Y, Pan L. Surface Selenization Strategy for V$_2$CT$_x$ MXene toward Superior Zn-Ion Storage. ACS Nano. 2022;16(2):2711. https://doi.org/10.1021/acsnano.1c09639.

[40] Tang YC, Zhao ZB, Wang YW, Dong YF, Liu Y, Wang XZ, Qiu JS. Carbon-stabilized interlayer-expanded few-layer MoSe$_2$ nanosheets for sodium ion batteries with enhanced rate capability and cycling performance. ACS Appl Mater Interfaces. 2016;8(47):32324. https://doi.org/10.1021/acsami.6b11230.

[41] Luo ZG, Zhou J, Wang LR, Fang GZ, Pan AQ, Liang SQ. Two-dimensional hybrid nanosheets of few layered MoSe$_2$ on reduced graphene oxide as anodes for long-cycle-life lithium-ion batteries. J Mater Chem A. 2016;4(40):15302. https://doi.org/10.1039/C6TA04390A.

[42] Yin JY, Hai PQ, Gao Y, Gan ZH, Wu C, Cheng YH, Xu X. Theory-driven designed TiO$_2$@MoO$_2$ heterojunction: balanced crystallinity and nanostructure toward desirable kinetics and high-rate sodium-ion storage. Nano Res. 2022. https://doi.org/10.1007/s12274-022-5120-x.

[43] Wu YC, Liu WR. Few-layered MoSe$_2$ ultrathin nanosheets as anode materials for lithium ion batteries. J Alloys Compd. 2020; 813:152074. https://doi.org/10.1016/j.jallcom.2019.152074.

[44] Yin Y, Zhang YM, Gao TL, Yao T, Zhang XH, Han JC, Wang XJ, Zhang ZH, Xu P, Zhang P. Synergistic phase and disorder engineering in 1T-MoSe$_2$ nanosheets for enhanced hydrogen-evolution reaction. Adv Mater. 2017;29(28):1700311. https://doi.org/10.1002/adma.201700311.

[45] Jiang M, Zhang JJ, Wu MH, Jian WJ, Xue HT, Ng TW, Lee CS, Xu J. Synthesis of 1T-MoSe$_2$ ultrathin nanosheets with an expanded interlayer spacing of 1.17 nm for efficient hydrogen evolution reaction. J Mater Chem A. 2016;4(39):14949. https://doi.org/10.1039/C6TA07020E.

[46] Xiao Y, Zhou MY, Liu JL, Xu J, Fu L. Phase engineering of two-dimensional transition metal dichalcogenides. Sci China Mater. 2019;62(6):759. https://doi.org/10.1007/s40843-018-9398-1.

[47] Qian J, Wang T, Xi B, Xi P, Gao D. Zn-doped MoSe$_2$ nanosheets as high-performance electrocatalysts for hydrogen evolution reaction in acid media. Electrochim Acta. 2019;296: 701. https://doi.org/10.1016/j.electacta.2018.10.089.

[48] Zhang C, Fei B, Yang D, Zhan H, Wang J, Diao J, Li J, Henkelman G, Cai D, Biendicho JJ. Robust lithium-sulfur batteries enabled by highly conductive WSe$_2$-based superlattices with tunable interlayer space. Adv Funct Mater. 2022;32(24): 2201322. https://doi.org/10.1002/adfm.202201322.

[49] Wang YY, Zhang X, Liu YJ, Zhao YB, Xie C, Song YX, Yang P. Crystallinity, phase controlling of g-C$_3$N$_4$/CdS hetrostructures towards high efficient photocatalytic H$_2$ generation. Int J Hydrogen Energy. 2019;44(57):30151. https://doi.org/10.1016/j.ijhydene.2019.09.181.

[50] Shan YB, Yue XF, Chen JJ, Han JK, Ekoya G, Hu LG, Liu R, Qiu ZJ, Cong CX. Revealing layer-dependent interlayer interactions by doping effect on graphene in WSe$_2$/N-layer graphene heterostructures using Raman and photoluminescence spectroscopy. Rare Met. 2022;41(11):3646. https://doi.org/10.1007/s12598-022-02053-7.

[51] Ma L, Zhang L, Wang D, Xin H, Ma Q. Pore structure evolution during lean-oxygen combustion of pyrolyzed residual from low-rank coal and its effect on internal oxygen diffusion mechanism. Fuel. 2022;319:123850. https://doi.org/10.1016/j.fuel.2022.123850.

[52] Gong J, Zhang ZY, Xi SB, Wang WJ, Lu JM, Chen P. Graphene quantum dot enabled interlayer spacing and electronic structure regulation of single-atom doped MoS$_2$ for efficient alkaline hydrogen evolution. Chem Eng J. 2023;451:138951. https://doi.org/10.1016/j.cej.2022.138951.

[53] Hyeongi K, Nguyen QH, Il TK, Jaehyun H. Scalable synthesis of high-performance molybdenum diselenide-graphite nanocomposite anodes for lithium-ion batteries. Appl Surf Sci. 2019;481: 1196. https://doi.org/10.1016/j.apsusc.2019.03.165.

[54] He H, Zhang H, Huang D, Kuang W, Li X, Hao J, Guo Z, Zhang C. Harnessing plasma-assisted doping engineering to stabilize

metallic phase MoSe$_2$ for fast and durable sodium-ion storage. Adv Mater. 2022;34(15):2200397. https://doi.org/10.1002/adma.202200397.

[55] Wang X, Zhang S, Shan Y, Chen L, Gao G, Zhu X, Cao B, He X. In situ heterogeneous interface construction boosting fast ion/electron transfer for high-performances lithium/potassium storage. Energy Storage Mater. 2021;37:55. https://doi.org/10.1016/j.ensm.2021.01.027.

[56] Xia Q, Zhao L, Li D, Wang J, Liu L, Hou C, Liu X, Xu H, Dang F, Zhang J. Phase modulation of 1T/2H MoSe$_2$ nanoflowers for highly efficient bifunctional electrocatalysis in rechargeable Li–O$_2$ batteries. J Mater Chem A. 2021;9(35):19922. https://doi.org/10.1039/D1TA03584C.

[57] Li Z, Cao YJ, Li GY, Chen L, Xu WY, Zhou MJ, He BH, Wang W, Hou ZH. High rate capability of S-doped ordered mesoporous carbon materials with directional arrangement of carbon layers and large d-spacing for sodium-ion battery. Electrochim Acta. 2021;366:137466. https://doi.org/10.1039/D1TA03584C.

[58] Zhou R, Wang H, Chang J, Yu C, Dai H, Chen Q, Zhou J, Yu H, Sun G, Huang W. Ammonium intercalation induced expanded 1T-rich molybdenum diselenides for improved lithium ion storage. ACS Appl Mater Interfaces. 2021;13(15):17459. https://doi.org/10.1021/acsami.0c22923.

[59] Zhang X, Xiong Y, Dong M, Hou Z, Qian Y. Construction of hierarchical MoSe$_2$@C hollow nanospheres for efficient lithium/sodium ion storage. Inorg Chem Front. 2020;7(8):1691. https://doi.org/10.1039/D0QI00017E.

[60] Dey S, Mujib SB, Singh G. Enhanced Li-ion rate capability and stable efficiency enabled by MoSe$_2$ nanosheets in polymer-derived silicon oxycarbide fiber electrodes. Nanomaterlals. 2022;12(3):553. https://doi.org/10.3390/nano12030553.

[61] Kang J, Su Q, Feng H, Huang P, Du G, Xu B. MoSe$_2$ nanosheets-wrapped flexible carbon cloth as binder-free anodes for high-rate lithium and sodium ion storages. Electrochim Acta. 2019;301:29. https://doi.org/10.1016/j.electacta.2019.01.136.

[62] Wei L, Zheng S, Qin A, Liao L, Chen S, Zhang K. 2D Hybrid nanostructures of MoSe$_2$⊥Sisal fiber activated carbon for enhanced Li storage performance. Mater Express. 2020;10(6):964. https://doi.org/10.1166/mex.2020.1740.

[63] Hai NQ, Kim H, Yoo IS, Kim JH, Hur J. Comparative study of mechanically milled MoS$_2$ and MoSe$_2$ in graphite matrix as anode materials for high-performance lithium-ion batteries. J Nanosci Nanotechnol. 2018;18(9):6469. https://doi.org/10.1166/jnn.2018.15667.

[64] Hao Q, Cui G, Zhao Y, Bakenov Z. Flower-like MoSe$_2$/MoO$_2$ composite with high capacity and long-term stability for lithium-ion battery. Nanomaterlals. 2019;9(9):1256. https://doi.org/10.3390/nano9091256.

[65] Guo M, Zhu X, Li M, Zhu J, Huang G, Li Y. Electrostatic self-assembly preparation of three-dimensional graphene coated red phosphorus for lithium-ion battery anode. Chin J Rare Met. 2022;46(8):1048. https://doi.org/10.13373/j.cnki.cjrm.XY21050015.

[66] Gao P, Zeng Y, Tang P, Wang Z, Yang J, Hu A, Liu J. Understanding the synergistic effects and structural evolution of Co(OH)$_2$ and Co$_3$O$_4$ toward boosting electrochemical charge storage. Adv Funct Mater. 2022;32(6):2108644. https://doi.org/10.1002/adfm.202108644.

[67] Yu Y, Hu X, Wang S, Qiao H, Liu Z, Song K, Shen X. High mass loading Ni$_4$Co$_1$-OH@CuO core-shell nanowire arrays obtained by electrochemical reconstruction for alkaline energy storage. Nano Res. 2022;15:685. https://doi.org/10.1007/s12274-021-3547-0.

[68] Chen L, Li Z, Li GY, Zhou MJ, He BH, Ouyang J, Xu WY, Wang W, Hou ZH. A facile self-catalyzed CVD method to synthesize Fe$_3$C/N-doped carbon nanofibers as lithium storage anode with improved rate capability and cyclability. J Mater Sci Technol. 2020;44:229. https://doi.org/10.1016/j.jmst.2019.11.013.

[69] Hu C, Chen L, Hu YJ, Chen AP, Chen L, Jiang H, Li CZ. Light-motivated SnO$_2$/TiO$_2$ heterojunctions enabling the breakthrough in energy density for lithium-ion batteries. Adv Mater. 2021;33(49):2103558. https://doi.org/10.1002/adma.202103558.

[70] Dong Y, Jiang H, Deng Z, Hu Y, Li C. Synthesis and assembly of three-dimensional MoS$_2$/rGO nanovesicles for high-performance lithium storage. Chem Eng J. 2018;350:1066. https://doi.org/10.1016/j.cej.2018.06.044.

[71] Guo Y, Zhang L. Research progress in synthesis and electrochemical performance of cobalt sulfide as anode material for secondary batteries. Chin J Rare Met. 2022;46(2):227. https://doi.org/10.13373/j.cnki.cjrm.XY20050006.

[72] Feng C, Wang W, Chen X, Wang S, Guo Z. Synthesis and electrochemical properties of ZnMn$_2$O$_4$ anode for lithium-ion batteries. Electrochim Acta. 2015;178:847. https://doi.org/10.1016/j.electacta.2015.08.070.

[73] Pasumarthi V, Liu TF, Dupuis M, Li C. Charge carrier transport dynamics in W/Mo-doped BiVO$_4$: first principles-based mesoscale characterization. J Mater Chem A. 2019;7(7):3054. https://doi.org/10.1039/C8TA09899A.

[74] Biswas P, Xu F, Ghildiyal P, Zachariah MR. In-situ thermochemical shock-induced stress at the metal/oxide interface enhances reactivity of aluminum nanoparticles. ACS Appl Mater Interfaces. 2022;14(23):26782. https://doi.org/10.1021/acsami.2c05412.

[75] Dou YH, Yuan D, Yu LP, Zhang WP, Zhang L, Fan KC, Al-Mamun M, Liu PR, He CT, Zhao HJ. Interpolation between W dopant and Co vacancy in CoOOH for enhanced oxygen evolution catalysis. Adv Mater. 2022;34(2):2104667. https://doi.org/10.1002/adma.202104667.

[76] Ghosh S, Kadam SR, Kolatkar S, Neyman A, Singh C, Enyashin AN, Bar Ziv R, Bar SM. W doping in Ni$_{12}$P$_5$ as a platform to enhance overall electrochemical water splitting. ACS Appl Mater Interfaces. 2021;14(1):581. https://doi.org/10.1021/acsami.1c16755.

[77] Jiao SL, Fu XW, Huang HW. Descriptors for the Evaluation of Electrocatalytic Reactions: d-Band Theory and Beyond. Adv Funct Mater. 2022;32(4):2107651. https://doi.org/10.1002/adfm.202107651.